OPTICS

Full-field imaging of thermal and acoustic dynamics in an individual nanostructure using tabletop high harmonic beams

Robert M. Karl Jr.*, Giulia F. Mancini*, Joshua L. Knobloch, Travis D. Frazer, Jorge N. Hernandez-Charpak, Begoña Abad, Dennis F. Gardner, Elisabeth R. Shanblatt, Michael Tanksalvala, Christina L. Porter, Charles S. Bevis, Daniel E. Adams, Henry C. Kapteyn, Margaret M. Murnane

Imaging charge, spin, and energy flow in materials is a current grand challenge that is relevant to a host of nanoenhanced systems, including thermoelectric, photovoltaic, electronic, and spin devices. Ultrafast coherent x-ray sources enable functional imaging on nanometer length and femtosecond timescales particularly when combined with advances in coherent imaging techniques. Here, we combine ptychographic coherent diffractive imaging with an extreme ultraviolet high harmonic light source to directly visualize the complex thermal and acoustic response of an individual nanoscale antenna after impulsive heating by a femtosecond laser. We directly image the deformations induced in both the nickel tapered nanoantenna and the silicon substrate and see the lowest-order generalized Lamb wave that is partially confined to a uniform nanoantenna. The resolution achieved—sub–100 nm transverse and 0.5-Å axial spatial resolution, combined with ≈10-fs temporal resolution—represents a significant advance in full-field dynamic imaging capabilities. The tapered nanoantenna is sufficiently complex that a full simulation of the dynamic response would require enormous computational power. We therefore use our data to benchmark approximate models and achieve excellent agreement between theory and experiment. In the future, this work will enable three-dimensional functional imaging of opaque materials and nanostructures that are sufficiently complex that their functional properties cannot be predicted.

INTRODUCTION

Microscopic imaging is critical for discovery and innovation in science and technology, accelerating advances in materials, bio, nano, and energy sciences, as well as in nanoelectronics, data storage, and medicine. In the deep nanoscale regime (<100 nm), bulk macroscopic models can no longer accurately predict heat, charge or spin transport, or the properties of doped or nanostructured materials (*1*–*4*). As a result, smart design of functional nanosystems has been challenging to date. To address this challenge, there is a critical need for new techniques that can image with high spatial and temporal resolution to enable a better understanding of fundamental nanoscale behavior and better design of energy-efficient next-generation devices (*5*–*7*).

Fortunately, all areas of imaging science, from electron to visible to x-ray, are undergoing revolutionary advances. Advances in ultrafast electron sources have recently enabled the direct visualization of out-of-equilibrium intermediate states in systems undergoing deformation and phase transitions on femtosecond timescales with high spatial resolution (*8*, *9*). Short-wavelength extreme ultraviolet (EUV) and soft x-ray beams also have unique capabilities for imaging because they can penetrate optically opaque materials, provide inherent chemical and magnetic contrast, and nondestructively image materials systems (*10*–*17*). By harnessing the new availability of ultrafast coherent x-ray free electron laser (XFEL) sources combined with coherent diffractive imaging (CDI) techniques (*18*), it is now possible to visualize the three-dimensional (3D) evolution of acoustic phonons in single nanocrystals (*19*, *20*) or the dislocation dynamics in battery nanoparticles due to cycling (*21*). Most of these approaches, however, have been limited in temporal resolution because of the natural pulse chirp of ultrafast electron bursts or by the intrinsic jitter of the ultrafast XFEL sources.

High harmonic generation (HHG) produces ultrafast, short-wavelength beams that are perfectly synchronized to the driving laser, with sub-femtosecond precision. Recent advances used HHG beams to uncover new regimes of nanoscale thermal transport (*2*), to distinguish between electron-electron screening and scattering (*22*), and to identify a new super-excited spin state in magnetic materials that emerges on timescales of <20 fs that traditional spectroscopies are blind to (*23*). However, most HHG measurements to date used spatially averaged spectroscopic measurements of either multiple nanostructures or uniform materials. Recently, the high spatial coherence of HHG beams has been harnessed to demonstrate the first full-field imaging with subwavelength spatial resolution using any x-ray source, small or large, with a spatial resolution of 12.6 nm (*14*).

Here, we combine ptychographic CDI with an EUV high harmonic light source to implement a stroboscopic movie of the complex, impulsive response of an individual nanostructure irradiated by an ultrafast laser pulse. Specifically, we image two nanoantennas of different shapes and achieve a sub–100 nm transverse resolution, a 0.5-Å axial precision, and ≈10-fs temporal resolution. In a tapered nanoantenna, we directly visualize thermal and acoustic displacements launched in both the nanostructure and the substrate. In a uniform nanoantenna, we measure the lowest-order generalized Lamb wave, a dispersive waveguided mode that is mostly confined to the nanostructure. We demonstrate that our data can be reliably

JILA, University of Colorado, 440 UCB, Boulder, CO 80309-0440, USA.
*Corresponding author. Email: robert.karl@colorado.edu (R.M.K.); giulia.mancini@colorado.edu (G.F.M.)

used to benchmark an approximate solution for the dynamic response of the 3D tapered nanoantenna, which cannot be modeled from first principles due to the enormous computational power required. In the future, this approach can be used to dynamically image 3D structures that cannot be simulated or to capture transport in complex nanoelectronic devices. Moreover, when extended to shorter wavelengths with higher penetration powers and spatial resolution, this work will enable functional imaging of the fastest dynamics in opaque materials and nanostructures.

EXPERIMENTAL SETUP AND METHODOLOGY

A schematic of the dynamic, ptychographic CDI microscope illuminated by tabletop high harmonic EUV light is shown in Fig. 1A. The EUV probe beam was produced by focusing an infrared (IR; 780 nm) 23-fs, 1.5-mJ, 5-kHz Ti:Sapphire laser pulse into a gas-filled waveguide. Part of the IR laser beam was used to induce thermal and acoustic dynamics in two different nickel nanostructures—a tapered nanoantenna and a uniform nanoantenna. For both samples, the dynamic response was captured by collecting stroboscopic images as a function of time delay between the IR laser pump and EUV probe pulses, essentially acquiring snapshots of a nanoscale movie. The acoustic and thermal dynamics are entirely reversible, with full relaxation of the sample between each IR pump pulse (see the Supplementary Materials). At each time delay, the sample was imaged using ptychographic CDI (*24*–*26*), which collects diffraction patterns from multiple overlapping fields of view to simultaneously reconstruct both the amplitude and phase of both the sample and the illuminating beam (*27*). Ptychographic imaging is a very robust form of CDI—it uses redundant information collected from the intensity of the scatter patterns from multiple overlapping fields of view to retrieve the missing phase information. Each amplitude image of the sample exhibits quantitative sensitivity to material composition (*13*), while each phase image is sensitive to both material composition and topography. The phase image is used to obtain a series of 2D+1 reconstructions; that is, 2D transverse full-field images combined with 1D axial (topographical) information, of acoustic wave propagation and thermal transport in the nanoantenna in response to laser-driven excitation. In Fig. 1 (B and C), we display a representative amplitude image and a 2D+1 phase image of the tapered nanoantenna taken at 35 ps before the arrival of the IR pump pulse ($t = 0$). We note that the reconstructions of the tapered nanoantenna entailed >2500 diffraction pattern measurements, including both dynamic images and a static reference. This required the HHG source to be extremely stable over the entire course of the experiment [>24 hours, limited by the data transfer time from the charge-coupled device (CCD)]. We note that although the thermal and acoustic dynamics probed in this work are relatively slow, the HHG probe pulse itself is <10 fs in duration, given the 23-fs pulse duration of the driving laser pulses. Given that the precision of the pump-probe delay line is also <<10 fs, the time resolution in our movie is also ≈10 fs, and this can be easily extended to sub-femtosecond resolution, as has been demonstrated in numerous spectroscopic studies using HHG sources

To separate the dynamics of the nanostructure from those of the substrate, we segment the images by applying a histogram thresholding to the complex images. In this approach, shown in Fig. 2 (A to C), we create a 2D histogram of the real and imaginary parts of the complex image. The resulting histograms have two primary peaks, corresponding to the nickel nanoantenna and the silicon substrate, which are well separated in the complex plane (Fig. 2A). Changes in the relative angle between two peaks in the histograms

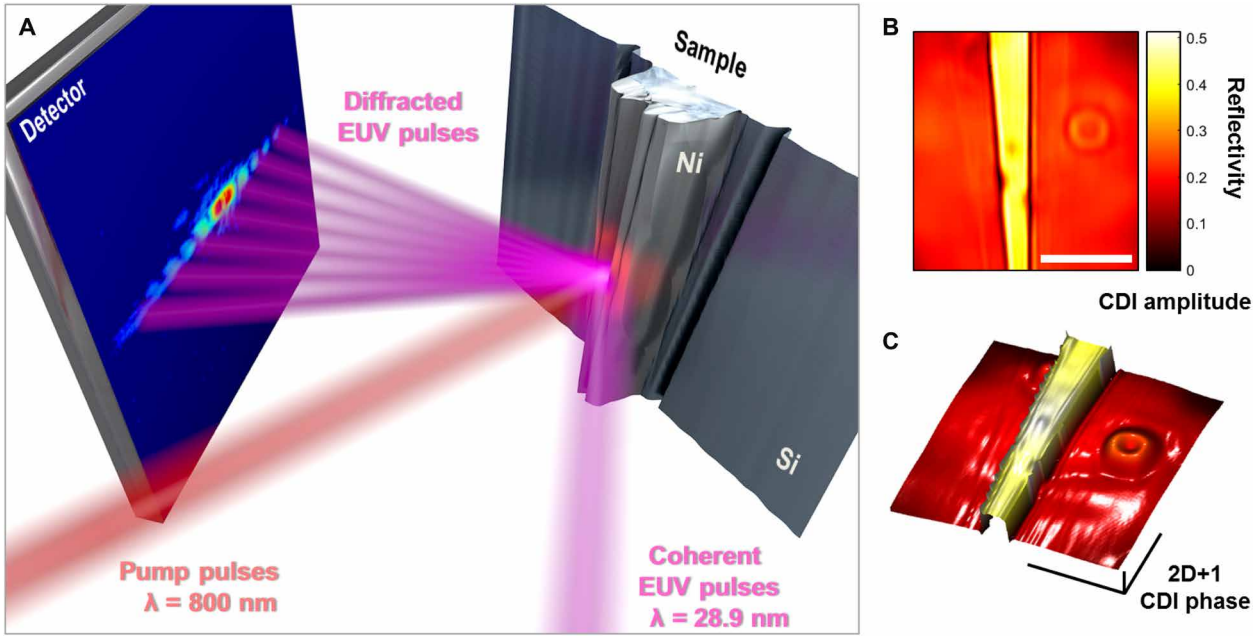

Fig. 1. Stroboscopic CDI microscope illuminated by 28.9-nm light from HHG. (**A**) Experimental layout. Dynamics are launched in a nickel tapered nanoantenna by an IR pump beam and are measured by an EUV probe beam. EUV light scattered from the sample is collected on an EUV-sensitive CCD. (**B**) Reconstructed, quantitative amplitude image. Scale bar, 5 μm. (**C**) Height map of the sample, obtained from the reconstructed phase image. Scale bars, 5 μm × 5 μm × 0.5 nm. The circular feature on the right in (B) and (C) is another nanostructure that is not investigated here.

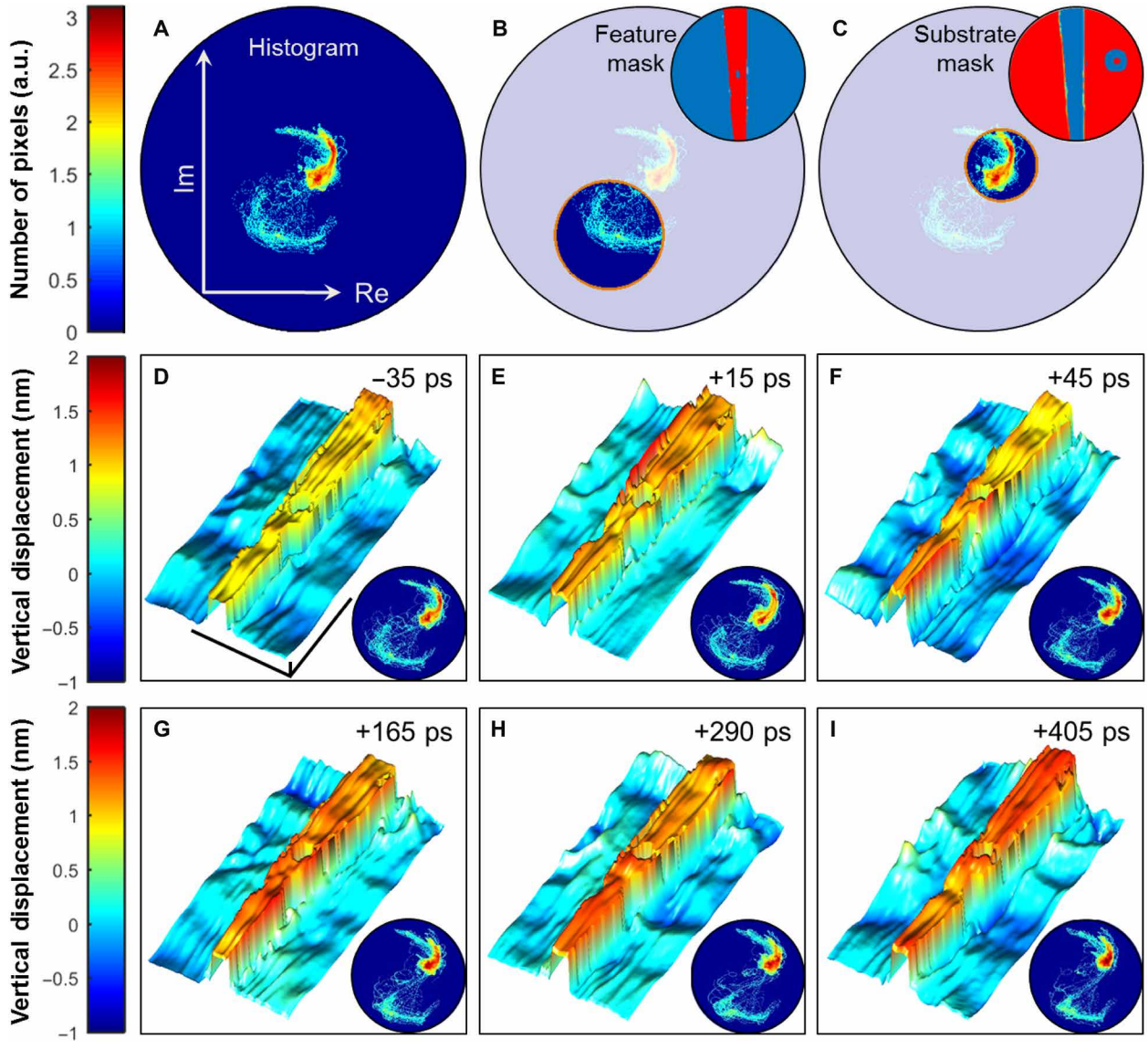

Fig. 2. Dynamic imaging of acoustic waves in an individual nanostructure. (**A**) Complex histogram analysis of the reconstructed image at $t = -35$ ps plotted on a nonlinear scale. Features can be masked to selectively probe dynamics of the nickel feature and of the silicon substrate. (**B**) Feature mask. (**C**) Substrate mask: Note that the substrate mask excludes the circular nanostructure shown in Fig.1 (B and C). (**D** to **I**) Reconstructed snapshots of the nickel nanostructure thermal expansion and subsequent propagation of acoustic waves in the substrate. All 2D+1 reconstructions are plotted on the same color scale. The scale bars indicated in (D) are 5 μm × 5 μm × 0.5 nm and are common to (D) to (I). An offset of 1 nm has been added to the nanostructure feature only, for visualization purposes. Insets: Dynamic histogram analysis. All histograms are plotted on the same color scale. Transient changes in the complex histogram are available in a stroboscopic movie in the Supplementary Materials. a.u., arbitrary units.

at each time delay (Fig. 2, D and I, insets) reflect changes in the relative phase between the nanoantenna and the substrate. We isolate these peaks to create two masks of the image: one of the nanoantenna (Fig. 2B) and one of the silicon substrate (Fig. 2C). Because we can isolate the parts of the sample that are from different materials, we can account for the material phase from the nickel and the silicon separately, leaving only the topographical phase, which can be directly converted into differences in height, yielding 2D+1 images of the sample.

To validate the time-resolved images from our microscope, we benchmarked our new technique to other well-established imaging modalities. We compared the static images to atomic force microscopy and scanning electron microscopy images. In addition, the reconstructed CDI amplitude images were verified with the literature values for the reflectivity of nickel and silicon (*12*). Furthermore, we validated the measured dynamics with spatially averaged measurements in a spectroscopic modality, following a similar approach to other studies (*2*, *28*), and compared those to the spatially resolved measurements. These multiple benchmarks validated both the spatial and temporal resolution of our dynamic imaging microscope.

DYNAMIC IMAGING RESULTS AND DISCUSSION

Representative 2D+1 images of the tapered nickel nanoantenna taken at several delay times are displayed in Fig. 2 (D to I), along with

complex histograms for each time frame. The complex images were reconstructed from the measured diffraction with a lateral resolution of 80 nm and with an axial precision of 0.5 Å. Each snapshot is the result of accounting for the height difference between the images taken with and without the laser excitation.

Dynamic height changes in specific regions of both the nanoantenna and the substrate can be directly visualized from the Fig. 2 movie frames. A movie containing all the image and histogram frames is available in the Supplementary Materials. The stroboscopic movie shows impulsive expansion at the edges of the structure (Fig. 2E), accompanied by a depression in the substrate immediately adjacent to the nanostructure, which reaches a maximum at time delays of ≈45 ps (Fig. 2F). At later time delays, the surface expansion of the nanostructure progressively propagates from the edges toward the center (Fig. 2, G to I). In addition, the onset of inhomogeneous changes at either end of the tapered nanoantenna can be observed at around +405 ps after the pump pulse, as the narrower end of the nanostructure undergoes a decrease in height, while the thicker end increases in height.

Next, we compare the experimentally measured dynamic response of the nanoantenna to an approximate finite element model of these complex dynamics (*28*, *29*). Implementing a complete simulation of the nanoscale thermal and acoustic response over the full 3D geometry of the tapered nanoantenna is computationally expensive due to the large aspect ratio (1:2500) and a volume of 1000 μm^3. Instead, we approximate the dynamics over a uniform 2.2 μm cross-section nanoantenna, which is a reasonable approximation because the opening angle of the nanoantenna is small. Figure 3 (A to D) shows the experimental scatter patterns from the tapered nanoantenna, which compares well to the simulated scattering pattern from the individual nanoline profile. In Fig. 3E, we plot the change in diffraction efficiency as a function of time to show good agreement between the experimental data (red) and the simulation (gray). Snapshots of acoustic wave propagation from the simulation (Fig. 3, F to I) show an initial thermal expansion, with larger contribution at the edges of the structure, followed by acoustic waves traveling both in the nanoantenna toward the center and into the silicon substrate, in remarkable agreement to what is directly observed in the reconstructed images. An additional simulation of a narrower nanoantenna with a 1.5-μm width was carried out to address the inhomogeneous height changes observed in the tapered nanoantenna at later time delays (Fig. 2I). These simulations suggest that the dynamics vary spatially, in agreement to the reconstructed images.

Finally, we demonstrate that it is possible to extract the acoustic wave velocity from the experimental data. To perform this characterization, we measured the diffraction from a uniform nanoantenna as a function of time delay, in 5-ps increments. A ptychographic reconstruction of the uniform nanoantenna multiplied by the illuminating

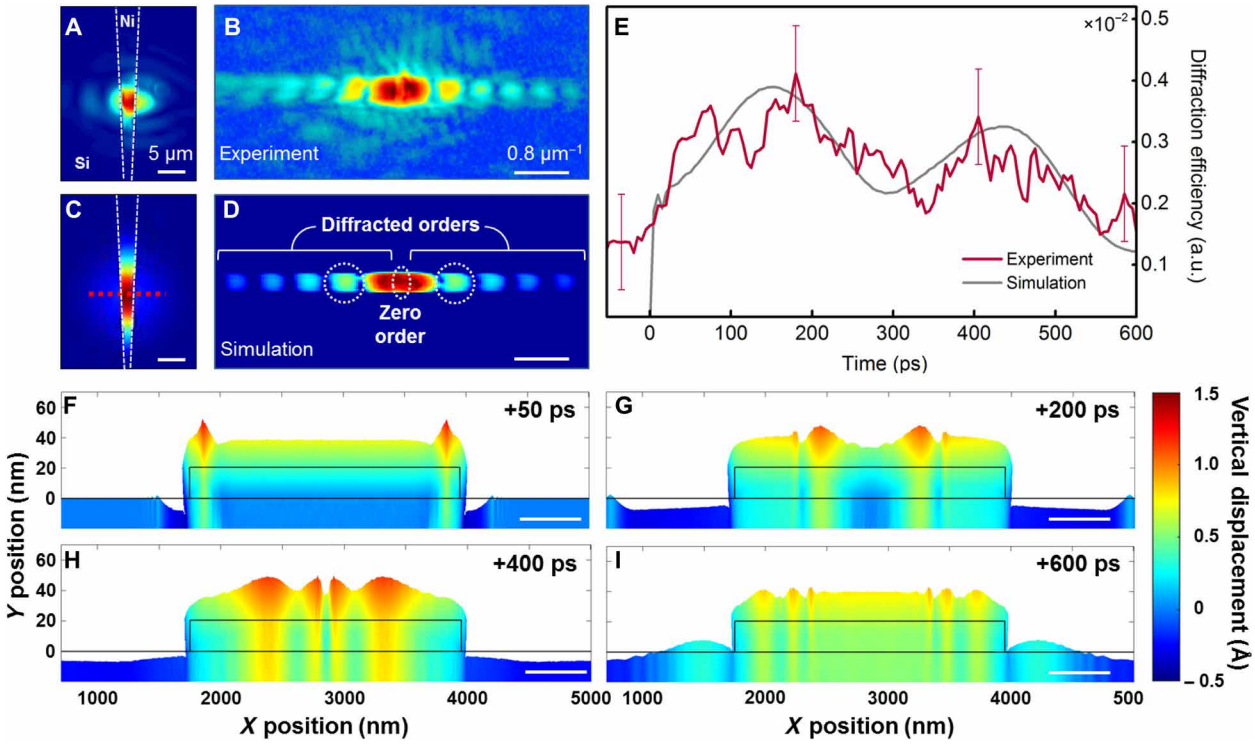

Fig. 3. Time-resolved EUV diffraction from an individual nanostructure compared to simulations. (**A**) Amplitude reconstruction of the nickel tapered nanoantenna on the silicon substrate multiplied by the reconstructed EUV beam (28.9 nm) at the sample. (**B**) Experimental diffraction pattern. (**C**) Simulation of the nickel nanoantenna on the silicon substrate, including the EUV illumination beam, which reflects more strongly from nickel than silicon. (**D**) Simulated diffraction pattern from the cross section of the nanostructure marked with the red dashed line in (C). (**E**) Transient diffraction efficiency into the marked diffracted orders (white dashed circles), relative to the undiffracted light (zero order) as a function of time, compared to the light diffracted from the unexcited sample. The experimental signal (red solid line) was smoothed over 11 time steps for clarity and is compared to the results obtained from the simulation (gray solid line). Error bars are derived from the standard deviation of the unsmoothed experimental data. (**F** to **I**) Snapshots of the simulation at four time delays (50, 200, 400, and 600 ps after laser-driven excitation), showing the thermal response and subsequent propagation of acoustic waves on the nickel nanostructure and also in the silicon substrate. These snapshots of the lineout correspond to the planes indicated in Fig. 4D, and they have been exaggerated by a factor of 250 in the vertical direction for clarity.

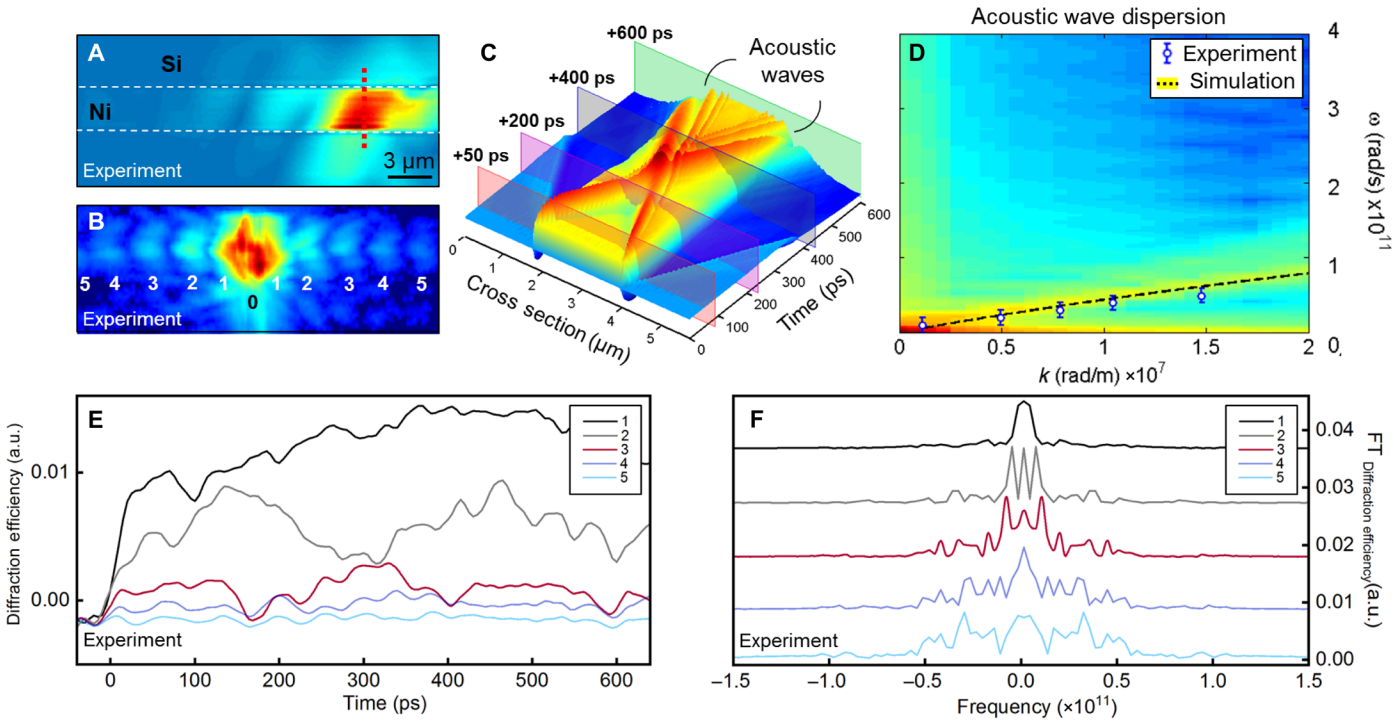

Fig. 4. Acoustic wave dispersion in an individual uniform nanoantenna. (**A**) Reconstructed amplitude image of the uniform nickel nanoantenna multiplied by the reconstructed probe. The red dashed line indicates the 2.2-μm cross section considered for the nanoline simulation. (**B**) Experimental diffraction pattern from the uniform nanoantenna indicating the undiffracted light (0) and the diffracted orders (1 to 5). (**C**) Simulation of a 2.2-μm cross section of the nickel nanoline as a function of time. Lineouts of the simulation at various time delays are shown in Fig.3 (F to I). (**D**) The dispersion of the acoustic waves can be calculated from the time-dependent simulation by Fourier transforming—in both time and space—the vertical surface displacement over the nanoline. The dispersion of the lowest-order generalized Lamb wave was also calculated via modal analysis of the nanoline (black dashed curve) and is in agreement with the experimental dispersion relation from the uniform nanoantenna (blue dots), which has a slope of 2790 ± 240 m/s. (**E** and **F**) Transient diffraction efficiencies relative to the light diffracted from the unexcited sample (E) and corresponding Fourier components (F) for each diffraction order obtained from the analysis of the uniform nanoantenna diffraction pattern.

probe is shown in Fig. 4A. This yields the diffraction pattern shown in Fig. 4B. The diffraction efficiency dynamics are shown for the first five diffracted orders in Fig. 4E. The temporal spectrum is calculated for each order by taking the Fourier transform of the portion of the traces after time zero (Fig. 4F). The oscillation frequency for each order is calculated by finding the lowest frequency peak in each spectrum. The spatial frequency for each order is determined by calculating the centroid of each diffraction peak. From these measurements, we can extract the dispersion of the surface acoustic waves (blue data points in Fig. 4D). The experimental dispersion relation yields an acoustic wave velocity of 2970 ± 240 m/s, which is between the Rayleigh velocity of thin-film nickel and that of silicon. Our analysis was further verified by measuring the dispersion of a known diffraction grating.

To verify the extracted surface acoustic wave dispersion, we use numerical simulations (Fig. 4C) in two approaches: analyze our time-dependent simulations and perform a modal analysis. The dispersion can be extracted from the time-dependent uniform nanoline simulations by Fourier transforming—in both time and space—the vertical surface displacement over the nanoline (*30*), resulting in the colormap seen in Fig. 4D. In addition, we performed finite-element modal analysis of a nickel film on a silicon substrate, resulting in the black dashed curve seen in Fig. 4D. The overlaid experimental dispersion agrees well with both numerically calculated dispersions. We remark that the modal analysis is not a fit to the data; rather, it is an independent simulation that corroborates the agreement between theory and experiment. From the modal analysis, we see that the surface acoustic waves propagating across the nanoline are coupled into dispersive waveguide modes, known as generalized Lamb waves, where the thin uniform nanoantenna acts as an acoustic waveguide (*31*). Because waveguide modes at these wavelengths are only partially confined to the nickel structure, the theoretical velocity lies between the Rayleigh velocity of nickel and that of silicon. The verification of this experimental dispersion demonstrates that it is possible to extract the acoustic velocity of individual nanostructures, and thus their elastic properties.

CONCLUSION

In summary, we have demonstrated a dynamic, full-field, tabletop EUV microscope that can capture the thermal and acoustic dynamics in individual nanoantennas, as well as those in the substrate. Furthermore, using stroboscopic EUV microscopy, we directly extract the dispersion of the acoustic waves in a uniform nickel nanoantenna. We note that this nanostructure shape is too complex to model from first principles; thus, dynamic imaging is the only way to visualize the complex thermal and acoustic response. In the future, this approach will enable 3D functional imaging of the fastest coupled charge, lattice, and spin dynamics in opaque materials and nanostructures that are sufficiently complex that their functional properties cannot be predicted.

MATERIALS AND METHODS

Experimental design

The 23-fs pulses were produced from a mode-locked Ti:Sapphire oscillator (KMLabs Griffin) and amplified in a multipass amplifier (KMLabs Dragon). These pulses were split into two arms: the pump arm and the probe arm. The pump arm contained a delay stage to control the timing between the pump and probe. The pump light was focused onto the sample near normal incidence, with a full width at half maximum (FWHM) of 650 μm. The intensity of the pump beam was 100 mW, making the fluence of the pump used in the experiments 8.4 mJ/cm^2.

To produce the EUV light through the HHG process, the probe arm was focused through a glass capillary filled with 44.5 torr of argon. Most of the IR light was rejected via a pair of super-polished silicon mirrors set near Brewster's angle. The residual IR light was attenuated by a 100-nm aluminum filter. A single harmonic at 28.9 nm was selected by steering the beam off of a pair of narrow-pass multilayer mirrors set at 45°. The EUV beam was then focused using a 5°, off-axis ellipsoidal mirror to a spot size of 7-μm FWHM, incident at 60° from the normal of the sample plane. To attenuate the IR pump light, a 195-nm-thick aluminum filter (Luxel) was placed before the CCD sensor (PI-MTE), which was placed 36.5 mm away from the sample plane. In this overall geometry, the highest theoretical resolution attainable due to the numeric aperture of the system is 38.1 nm.

To characterize the long-term stability of the probing 28.9-nm harmonic light, the direct beam was measured on the detector every 1.5 s for an hour. The standard deviation of the centroid of the beam on the camera was 1.9 and 0.11% of the beam diameter in the vertical and horizontal, respectively. This was a sufficient level of stability as each ptychographic scan took 20 min to acquire. However, the stability of the system extended well beyond the 1 hour of dedicated stability measurements, which was confirmed by acquiring ptychographic scans 3 days apart and reconstructing nearly identical probes.

Stroboscopic imaging was conducted at room temperature in reflection geometry, with the background pressure in the experimental vacuum chamber being ~10^{-7} mbar. For a single movie frame, the ptychographic CDI scan consists of 82 diffraction patterns recorded in a Fermat spiral pattern (*32*) with separations of 2 μm between adjacent positions. The data were collected with 2 × 2 on-chip binning, averaging over three accumulations, with a 200-kHz readout rate and a 0.15-s exposure time. Each image was created from a total of 49.2-s exposure from ~6×10^9 photons/s. The stroboscopic movie frames recorded with ptychographic CDI consisted of 14 different pump-probe delays. At each time delay, a differential measurement with and without the laser-driven excitation was carried out to account for fluctuations in the system. In addition, 10 images of the EUV beam reflected off of the bare silicon substrate were recorded for each measurement to apply the modulus-enforced probe constraint technique (*14*). We note that because the beam was reflected off of silicon, the diffraction patterns needed to be renormalized based on the reflectivity of silicon. The result is 28 images of the sample: 14 at different pump probe delays with respect to the pump pulse ($t = 0$) and 14 as reference images without the laser-driven excitation. The experimental movie of the nanostructure was reconstructed from >15 GB of raw data collected over a 14.5-hour period, which is a large amount of data for a tabletop-scale stroboscopic microscope.

For our experiment, we selected time delays such that the predominant dynamics observed in this experiment are the surface acoustic waves propagating within the nanostructure. We remark that this range can be extended at will to access the nanosecond-long thermal decay. Moreover, finer time steps can be taken to access high-frequency longitudinal acoustic waves propagating in the nanostructure and substrate, which have been extensively studied with spectroscopic techniques (*2*, *28*, *33*).

Sample preparation

The sample consisted of nickel nanostructures patterned with electron beam liftoff lithography on a silicon substrate. The tapered nanoantenna was characterized with optical microscopy, scanning electron microscopy (SEM), and atomic force microscopy (AFM), as displayed in fig. S1. The recovered reflectivity values of 0.024 ± 0.017 for the silicon substrate and of 0.16 ± 0.04 for the nickel feature are in agreement with tabulated values (*12*). The CDI phase image is in agreement with a height of 20 ± 2 nm estimated with AFM. We imaged an additional circular nanostructure to the right of the tapered nanoantenna. Its effect on the dynamic signal has been excluded by the histogram image segmentation.

SUPPLEMENTARY MATERIALS

Supplementary material for this article is available at http://advances.sciencemag.org/cgi/content/full/4/10/eaau4295/DC1

Histogram analysis
Diffraction efficiency
Image reconstructions
Dynamics simulation
Dispersion analysis
Fig. S1. Preliminary sample characterization.
Fig. S2. Histogram analysis.
Fig. S3. Reconstructed EUV beam.
Fig. S4. Comparison of the spatially resolved acoustic dynamics.
Fig. S5. Analysis of dispersion in a nickel grating on silicon substrate.
Table S1. Parameters for material properties used in the simulation.
Movie S1. Movie of the 2D+1 height maps form the phase reconstructions displayed as a function of time.
Movie S2. Movie of the complex histograms for each reconstruction.
Movie S3. Movies 1 and 2 displayed concurrently, allowing the relation between the images and the histograms to be visualized.
References (*34*–*48*)

REFERENCES AND NOTES

1. M. E. Siemens, Q. Li, R. Yang, K. A. Nelson, E. H. Anderson, M. M. Murnane, H. C. Kapteyn, Quasi-ballistic thermal transport from nanoscale interfaces observed using ultrafast coherent soft X-ray beams. *Nat. Mater.* **9**, 26–30 (2010).
2. K. Hoogeboom-Pot, J. N. Hernandez-Charpak, X. Gu, T. D. Frazer, E. H. Anderson, W. Chao, R. W. Falcone, R. Yang, M. M. Murnane, H. C. Kapteyn, D. Nardi, A new regime of nanoscale thermal transport: Collective diffusion increases dissipation efficiency. *Proc. Natl. Acad. Sci. U.S.A.* **112**, 4846–4851 (2015).
3. R. F. Wang, C. Nisoli, R. S. Freitas, J. Li, W. McConville, B. J. Cooley, M. S. Lund, N. Samarth, C. Leighton, V. H. Crespi, P. Schiffer, Artificial "spin ice" in a geometrically frustrated lattice of nanoscale ferromagnetic islands. *Nature* **439**, 303–306 (2006).
4. P. D. Antunez, D. M. Bishop, Y. Luo, R. Haight, Efficient kesterite solar cells with high open-circuit voltage for applications in powering distributed devices. *Nat. Energy* **2**, 884–890 (2017).
5. N. I. Zheludev, The road ahead for metamaterials. *Science* **328**, 582–583 (2010).
6. S. W. King, H. Simka, D. Herr, H. Akinaga, M. Garner, Research updates: The three M's (materials, metrology, and modeling) together pave the path to future nanoelectronic technologies. *APL Mater.* **1**, 040701 (2013).
7. K. A. Moler, Imaging quantum materials. *Nat. Mater.* **16**, 1049–1052 (2017).
8. B. Barwick, H. S. Park, O.-H. Kwon, J. S. Baskin, A. H. Zewail, 4D imaging of transient structures and morphologies in ultrafast electron microscopy. *Science* **322**, 1227–1231 (2008).
9. F. Carbone, O.-H. Kwon, A. H. Zewail, Dynamics of chemical bonding mapped by energy-resolved 4D electron microscopy. *Science* **325**, 181–185 (2009).
10. A. H. Chin, R. W. Schoenlein, T. E. Glover, P. Balling, W. P. Leemans, C. V. Shank, Ultrafast structural dynamics in InSb measured using time resolved X-ray diffraction. *Phys. Rev. Lett.* **83**, 336–339 (1999).

11. M. Khalil, M. A. Marcus, A. L. Smeigh, J. K. McCusker, H. H. W. Chong, R. W. Schoenlein, Picosecond X-ray absorption spectroscopy of a photoinduced iron(II) spin crossover reaction in solution. *J. Phys. Chem. A* **110**, 38–44 (2006).
12. The Center for X-Ray Optics, http://www.cxro.lbl.gov/.
13. E. R. Shanblatt, C. L. Porter, D. F. Gardner, G. F. Mancini, R. M. Karl Jr., M. D. Tanksalvala, C. S. Bevis, V. H. Vartanian, H. C. Kapteyn, D. E. Adams, M. M. Murnane, Quantitative chemically specific coherent diffractive imaging of reactions at buried interfaces with few nanometer precision. *Nano Lett.* **16**, 5444–5450 (2016).
14. D. F. Gardner, M. Tanksalvala, E. R. Shanblatt, X. Zhang, B. R. Galloway, C. L. Porter, R. Karl Jr., C. Bevis, D. E. Adams, H. C. Kapteyn, M. M. Murnane, G. F. Mancini, Subwavelength coherent imaging of periodic samples using a 13.5 nm tabletop high-harmonic light source. *Nat. Photonics* **11**, 259–263 (2017).
15. Z. Tao, M. Keller, M. Mavrikakis, H. Kapteyn, M. Murnane, Direct time-domain observation of attosecond final-state lifetimes in photoemission from solids. *Science* **353**, 62–67 (2016).
16. W. Chao, B. Harteneck, J. Liddle, E. Anderson, D. Attwood, Soft X-ray microscopy at a spatial resolution better than 15 nm. *Nature* **435**, 1210–1213 (2005).
17. M. Beckers, T. Senkbeil, T. Gorniak, M. Reese, K. Giewekemeyer, S.-C. Gleber, T. Salditt, A. Rosenhahn, Chemical contrast in soft X-ray ptychography. *Phys. Rev. Lett.* **107**, 208101 (2011).
18. J. Miao, T. Ishikawa, I. K. Robinson, M. M. Murnane, Beyond crystallography: Diffractive imaging using coherent x-ray light sources. *Science* **348**, 530–535 (2015).
19. J. N. Clark, L. Beitra, G. Xiong, A. Higginbotham, D. M. Fritz, H. T. Lemke, D. Zhu, M. Chollet, G. J. Williams, M. Messerschmidt, B. Abbey, R. J. Harder, A. M. Korsunsky, J. S. Wark, I. K. Robinson, Ultrafast three-dimensional imaging of lattice dynamics in individual gold nanocrystals. *Science* **341**, 56–59 (2013).
20. J. N. Clark, L. Beitra, G. Xiong, D. M. Fritz, H. T. Lemke, D. Zhu, M. Chollet, G. J. Williams, M. M. Messerschmidt, B. Abbey, R. J. Harder, A. M. Korsunsky, J. S. Wark, D. A. Reis, I. K. Robinson, Imaging transient melting of a nanocrystal using an X-ray laser. *Proc. Natl. Acad. Sci. U.S.A.* **112**, 7444–7448 (2015).
21. A. Ulvestad, A. Singer, J. N. Clark, H. M. Cho, J. W. Kim, R. Harder, J. Maser, Y. S. Meng, O. G. Shpyrko, Topological defect dynamics in operando battery nanoparticles. *Science* **348**, 1344–1348 (2015).
22. C. Chen, Z. Tao, A. Carr, P. Matyba, T. Szilvási, S. Emmerich, M. Piecuch, M. Keller, D. Zusin, S. Eich, M. Rollinger, W. You, S. Mathias, U. Thumm, M. Mavrikakis, M. Aeschlimann, P. M. Oppeneer, H. Kapteyn, M. Murnane, Distinguishing attosecond electron–electron scattering and screening in transition metals. *Proc. Natl. Acad. Sci. U.S.A.* **114**, 5300–5307 (2017).
23. P. Tengdin, W. You, C. Chen, X. Shi, D. Zusin, Y. Zhang, C. Gentry, A. Blonsky, M. Keller, P. M. Oppeneer, H. C. Kapteyn, Z. Tao, M. M. Murnane, Critical behavior within 20fs drives the out-of-equilibrium laser-induced magnetic phase transition in nickel. *Sci. Adv.* **4**, eaap9744 (2018).
24. A. M. Maiden, J. M. Rodenburg, An improved ptychographical phase retrieval algorithm for diffractive imaging. *Ultramicroscopy* **109**, 1256–1262 (2009).
25. A. Maiden, D. Johnson, P. Li, Further improvements to the ptychographical iterative engine. *Optica* **4**, 736–745 (2017).
26. P. Thibault, M. Dierolf, A. Menzel, O. Bunk, C. David, F. Pfeiffer, High-resolution scanning x-ray diffraction microscopy. *Science* **321**, 379–382 (2008).
27. P. Thibault, M. Dierolf, O. Bunk, A. Menzel, F. Pfeiffer, Probe retrieval in ptychographic coherent diffractive imaging. *Ultramicroscopy* **109**, 338–343 (2009).
28. J. N. Hernandez-Charpak, K. M. Hoogeboom-Pot, Q. Li, T. D. Frazer, J. L. Knobloch, M. Tripp, S. W. King, E. H. Anderson, W. Chao, M. M. Murnane, H. C. Kapteyn, D. Nardi, Full characterization of the mechanical properties of 11–50 nm ultrathin films: Influence of network connectivity on the Poisson's ratio. *Nano Lett.* **17**, 2178–2183 (2017).
29. COMSOL, *COMSOL Multiphysics Version 4.3b* (COMSOL, 2013).
30. D. M. Profunser, O. B. Wright, O. Matsuda, Imaging ripples on phononic crystals reveals acoustic band structure and Bloch harmonics. *Phys. Rev. Lett.* **97**, 055502 (2006).
31. B. A. Auld, *Acoustic Fields and Waves in Solids* (Wiley, 1973).
32. X. Huang, H. Yan, R. Harder, Y. Hwu, I. K. Robinson, Y. S. Chu, Optimization of overlap uniformness for ptychography. *Opt. Express* **22**, 12634–12644 (2014).
33. K. M. Hoogeboom-Pot, E. Turgut, J. N. Hernandez-Charpak, J. M. Shaw, H. C. Kapteyn, M. M. Murnane, D. Nardi, Nondestructive measurement of the evolution of layer-specific mechanical properties in sub-10 nm bilayer films. *Nano Lett.* **16**, 4773–4778 (2016).
34. D. F. Gardner, B. Zhang, M. D. Seaberg, L. S. Martin, D. E. Adams, F. Salmassi, E. Gullikson, H. Kapteyn, M. Murnane, High numerical aperture reflection mode coherent diffraction microscopy using off-axis apertured illumination. *Opt. Express* **20**, 19050–19059 (2012).
35. M. D. Seaberg, B. Zhang, D. F. Gardner, E. R. Shanblatt, M. M. Murnane, H. C. Kapteyn, D. E. Adams, Tabletop nanometer extreme ultraviolet imaging in an extended reflection mode using coherent Fresnel ptychography. *Optica* **1**, 39–44 (2014).
36. F. Zhang, I. Peterson, J. Vila-Comamala, A. Diaz, F. Berenguer, R. Bean, B. Chen, A. Menzel, I. K. Robinson, J. M. Rodenburg, Translation position determination in ptychographic coherent diffraction imaging. *Opt. Express* **21**, 13592–13606 (2013).
37. R. M. Goldstein, H. A. Zebker, C. L. Werner, Satellite radar interferometry: Two-dimensional phase unwrapping. *Radio Sci.* **23**, 713–720 (1988).
38. D. Ghiglia, M. Pritt, *Two-Dimensional Phase Unwrapping: Theory, Algorithms, and Software* (Wiley, 1998), 512 pp.
39. D. Nardi, M. Travagliati, M. E. Siemens, Q. Li, M. M. Murnane, H. C. Kapteyn, G. Ferrini, F. Parmigiani, F. Banfi, Probing thermomechanics at the nanoscale: Impulsively excited pseudosurface acoustic waves in hypersonic phononic crystals. *Nano Lett.* **11**, 4126–4133 (2011).
40. F. Banfi, F. Pressacco, B. Revaz, C. Giannetti, D. Nardi, G. Ferrini, F. Parmigiani, *Ab initio* thermodynamics calculation of all-optical time-resolved calorimetry of nanosize systems: Evidence of nanosecond decoupling of electron and phonon temperatures. *Phys. Rev. B Condens. Matter* **81**, 1–5 (2010).
41. J. Lian, S.-W. Lee, L. Valdevit, M. I. Baskes, J. R. Greer, Emergence of film-thickness- and grain-size-dependent elastic properties in nanocrystalline thin films. *Scr. Mater.* **68**, 261–264 (2013).
42. M. E. Siemens, Q. Li, M. M. Murnane, H. C. Kapteyn, R. Yang, E. H. Anderson, K. A. Nelson, High-frequency surface acoustic wave propagation in nanostructures characterized by coherent extreme ultraviolet beams. *Appl. Phys. Lett.* **94**, 093103 (2009).
43. D. Nardi, F. Banfi, C. Giannetti, B. Revaz, G. Ferrini, F. Parmigiani, Pseudosurface acoustic waves in hypersonic surface phononic crystals. *Phys. Rev. B Condens. Matter* **80**, 104119 (2009).
44. J. A. Dean, *Lange's Handbook of Chemistry* (McGraw-Hill Professional, 2005), 1424 pp.
45. T. G. Kollie, Measurement of the thermal-expansion coefficient of nickel from 300 to 1000 K and determination of the power-law constants near the Curie temperature. *Phys. Rev. B* **16**, 4872–4881 (1977).
46. Y. Okada, Y. Tokumaru, Precise determination of lattice parameter and thermal expansion coefficient of silicon between 300 and 1500 K. *J. Appl. Phys.* **56**, 314–320 (1984).
47. P. D. Desai, Thermodynamic properties of iron and silicon. *J. Phys. Chem. Ref. Data* **15**, 967–983 (1986).
48. M. A. Hopcroft, W. D. Nix, T. W. Kenny, What is the Young's modulus of silicon? *J. Microelectromech. Syst.* **19**, 229–238 (2010).

Acknowledgments

Funding: This work was supported by the NSF STC on Real-Time Functional Imaging (STROBE) (DMR 1548924), the Gordon and Betty Moore Foundation's EPiQS Initiative through grant GBMF 4538, and DARPA PULSE grant W31P4Q-13-1-0015. R.M.K. acknowledges support from an NDSEG Fellowship. C.S.B. acknowledges support from an NSF Fellowship. J.L.K. acknowledges support from an SRC Fellowship. **Author contributions:** H.C.K. and M.M.M. conceived the experiment. R.M.K. and G.F.M. collected and analyzed the datasets. J.L.K. performed the acoustic simulations. G.F.M. performed SEM and AFM experiments. E.R.S. and C.L.P. fabricated the samples. All authors designed aspects of the experiment and interpretation, performed the research, and wrote the paper. **Competing interests:** M.M.M. and H.C.K. have a financial interest in KMLabs. The authors declare no other competing interests. **Data and materials availability:** All data needed to evaluate the conclusions in the paper are present in the paper and/or the Supplementary Materials. Additional data related to this paper may be requested from the authors.

Submitted 09 June 2018
Accepted 12 September 2018
Published 19 October 2018
10.1126/sciadv.aau4295

Citation: R. M. Karl Jr., G. F. Mancini, J. L. Knobloch, T. D. Frazer, J. N. Hernandez-Charpak, B. Abad, D. F. Gardner, E. R. Shanblatt, M. Tanksalvala, C. L. Porter, C. S. Bevis, D. E. Adams, H. C. Kapteyn, M. M. Murnane, Full-field imaging of thermal and acoustic dynamics in an individual nanostructure using tabletop high harmonic beams. *Sci. Adv.* **4**, eaau4295 (2018).

Science Advances

Full-field imaging of thermal and acoustic dynamics in an individual nanostructure using tabletop high harmonic beams

Robert M. Karl, Jr., Giulia F. Mancini, Joshua L. Knobloch, Travis D. Frazer, Jorge N. Hernandez-Charpak, Begoña Abad, Dennis F. Gardner, Elisabeth R. Shanblatt, Michael Tanksalvala, Christina L. Porter, Charles S. Bevis, Daniel E. Adams, Henry C. Kapteyn and Margaret M. Murnane

Sci Adv **4** (10), eaau4295.
DOI: 10.1126/sciadv.aau4295